MOLECULAR IMAGING AND BIOLOGY

Mol Imaging Biol (2019) 21:1117–1126
DOI: 10.1007/s11307-019-01330-9

Published Online: 8 March 2019

WMIS World Molecular Imaging Society

Check for updates

RESEARCH ARTICLE

Metabolic Evaluation of *MYCN*-Amplified Neuroblastoma by 4-[^{18}F]FGln PET Imaging

Chao Li,[1] Shuo Huang,[1] Jun Guo,[1] Cheng Wang,[2] Zhichao Huang,[3] Ruimin Huang,[4,5] Liang Liu,[6] Sheng Liang,[1] Hui Wang[1]

[1]*Department of Nuclear Medicine, Xinhua Hospital, Shanghai Jiao Tong University, School of Medicine, 1665 Kongjiang Road, Shanghai, 200092, China*

[2]*Department of Nuclear Medicine, Renji Hospital, Shanghai Jiao Tong University, School of Medicine, 1630 Dongfang Road, Shanghai, 200127, China*

[3]*PINGSENG Healthcare, 999 Qujia Road, Kunshan, 215341, Jiangsu, China*

[4]*Shanghai Institute of Materia Medica, Chinese Academy of Sciences, 555 Zuchongzhi Road, Shanghai, 201203, China*

[5]*University of Chinese Academy of Sciences, No.19(A) Yuquan Road, Beijing, 100049, China*

[6]*Department of Cardiology, Shanghai Jiao Tong University Affiliated Sixth People's Hospital, 600 Yishan Road, Shanghai, 200233, China*

Abstract

Purpose: This study aims to explore whether 4-(2S,4R)-[^{18}F]fluoroglutamine (4-[^{18}F]FGln) positron emission tomography (PET) imaging is helpful in identifying and monitoring *MYCN*-amplified neuroblastoma by enhanced glutamine metabolism.

Procedures: Cell uptake studies and dynamic small-animal PET studies of 4-[^{18}F]FGln and 2-deoxy-2-[^{18}F]fluoro-D-glucose ([^{18}F]FDG) were conducted in human *MYCN*-amplified (IMR-32 and SK-N-BE (2) cells) and non-*MYCN*-amplified (SH-SY5Y cell) neuroblastoma cells and animal models. Subsequently, short hairpin RNA (shRNA) knockdown of alanine-serine-cysteine transporter 2 (*ASCT2/SLC1A5*) in IMR-32 cells and xenografts were investigated *in vitro* and *in vivo*. Western blot (WB), real-time polymerase chain reaction (RT-PCR), and immunofluorescence (IF) assays were used to measure the prevalence of ASCT2, Ki-67, and c-Caspase 3, respectively.

Results: IMR-32 and SK-N-BE (2) cells showed high glutamine uptake *in vitro* (31.6 ± 1.7 and 21.6 ± 6.6 %ID/100 μg). In the *in vivo* study, 4-[^{18}F]FGln was localized in IMR-32, SK-N-BE (2), and SH-SY5Y tumors with a high uptake (6.6 ± 0.3, 5.6 ± 0.2, and 3.7 ± 0.1 %ID/g). The maximum uptake (tumor-to-muscle, T/M) of the IMR-32 and SK-N-BE (2) tumors (3.71 and 2.63) was significantly higher than that of SH-SY5Y (1.54) tumors ($P < 0.001$, $P < 0.001$). The maximum uptake of 4-[^{18}F]FGln in IMR-32 and SK-N-BE (2) tumors was 2.3-fold and 2.1-fold higher than that of [^{18}F]FDG, respectively. Furthermore, in the *in vitro* and *in vivo* studies, the maximum uptake of 4-[^{18}F]FGln in shASCT2-IMR-32 cells and tumors was 2.1-fold and 2.5-fold lower than that of the shControl-IMR-32. No significant difference in [^{18}F]FDG uptake was found between shASCT2-IMR-32 and shControl-IMR-32 cells and tumors.

Conclusion: 4-[^{18}F]FGln PET can provide a valuable clinical tool in the assessment of metabolic glutamine uptake in *MYCN*-amplified neuroblastoma. ASCT2-targeted therapy may provide a supplementary method in *MYCN*-amplified neuroblastoma treatment.

Key Words: Glutamine, PET, *MYCN*, ASCT2, Neuroblastoma

Chao Li and Shuo Huang contributed equally to this work.

Correspondence to: Ruimin Huang; *e-mail:* rmhuang@simm.ac.cn, Sheng Liang; *e-mail:* liangsheng364214@163.com, Hui Wang; *e-mail:* wanghui@xinhuamed.com.cn

Introduction

Neuroblastoma is the most common extracranial solid tumor detected in childhood [1]. The amplification of the proto-oncogene *MYCN*-amplified is noted in 25 % of cases and is correlated with a high-risk disease and a poor prognosis, which is also considered as the best-characterized genetic marker of risk in NB [2]. Typically, tumor cells exhibit increased aerobic glycolysis (the Warburg effect) [3] for their demands for energy and biosynthesis. Many cancer cells also depend on glutamine as they use the glutaminolysis pathway to generate building blocks and energy for anabolic purposes [4]. Glutamine is transported into the cytosol by LAT1 (L-type amino acid transporters 1), ASCT2 (system ASC amino acid transporters 2), and other transporters. ASCT2 and LAT1 are upregulated in a variety of cancerous tissue [5, 6]. In addition, ASCT2 directly participates in cell survival signaling and plays an important role in driving the glutamine-dependent growth of the human neuroblastoma cell line SK-N-SH [7].

Myc drives glutamine uptake and catabolism by activating the expression of genes involved in glutamine metabolism, including glutaminase (GLS), ASCT2, and LAT1, which mediate the entry of glutamine into the glutaminolysis pathway [8–10]. It has been reported that *myc* regulates glutaminolysis in glioma cells and lymphoma cells and results in PI3K-independent glutamine to sustain cellular viability and the tricarboxylic acid cycle (TCA cycle) anaplerosis by activating the expression of ASCT2 and GLS1 [10, 11]. A study by Ren et al. [12, 13] showed that *MYCN*-amplified neuroblastoma cells constantly required large amounts of glutamine to support their unabated growth and predominantly relied on the activation of ASCT2 to maintain sufficient levels of glutamine, which is essential for the TCA cycle anaplerosis. Recently, it has been reported that the positron emission tomography (PET) imaging agent 4-[^{18}F]FGln, which targets glutamine uptake was applied in preclinical and clinical studies in oncology [14–19].

Given these findings, we hypothesized that glutamine metabolism measured by PET could be used as a precise imaging for biological evaluation of *MYCN*-amplified neuroblastoma.

Materials and Methods

Radiolabeling of 4-[^{18}F]FGln

The synthesis of 4-FGln and the radiosynthesis of 4-[^{18}F]FGln have been described by previous studies [14, 15]. The purity of 4-[^{18}F]FGln was determined by chiral high-performance liquid chromatography (HPLC) (Chirex 3126 D-penicillamine, 1 mM CuSO4 solution, 1 ml/min). The minimum specific activity of 4-[^{18}F]FGln at the end of synthesis was 45 mCi/μmol, the radiochemical purity (RCP) was > 95 %, and the optical purity was > 90 % (the results were derived from six separate experiments). 2-Deoxy-2-[^{18}F]fluoro-D-glucose ([^{18}F]FDG) was produced by our department using a conventional method, and the radiochemical purity of every batch of the drug was > 98 %.

Cell Culture

Non-*MYCN*-amplified cell lines (SH-SY5Y) and *MYCN*-amplified cell lines (SK-N-BE (2), IMR-32) were purchased from the Chinese Academy of Science and cultured in Dulbecco's Modified Eagle's Medium (DMEM, Gibco, 11995065) supplemented with 10 % foetal bovine serum (FBS; cat no. 10099141; Gibco), 2 mM glutamine (Gln) (cat no. 59202C; Sigma), and 1 % penicillin and streptomycin. The cells were maintained in a T-75 culture flask under humidified incubator conditions (37 °C, 5 % CO2) and were routinely passaged at confluence.

Cell Uptake and Protein Incorporation Studies In Vitro

SH-SY5Y cells, SK-N-BE (2) cells, IMR-32 cells, shASCT2-IMR-32 cells, and shControl-IMR-32 cells (1.0 × 105 cells/well) were attached to a 24-well plate overnight in the complete media. The cellular uptake was measured with these cells by using 4-[^{18}F]FGln and [^{18}F]FDG. On the day of the experiment, the media was aspirated and the cells were washed 3 times with 1 ml of a warm phosphate buffered saline (PBS, containing 0.90 mM of Ca2+ and 1.0 mM of Mg2+). The cells were incubated at 37 °C for 15, 30, 60, and 120 min with 37 kBq/well of 4-[^{18}F]FGln. Then, radioactive medium was removed and the cells were washed 3 times with 1 ml of ice cold PBS without $Ca^{2+}$and Mg^{2+}, treated with 0.25 % trypsin, and resuspended in PBS. After centrifugation (1500 rpm, 5 min), the supernatant was transferred to new tubes and the cells were suspended in 30 μl of 2 % sodium dodecyl sulphate (SDS). The radioactivity of both the supernatant and pellet was determined and measured with a gamma counter. The total protein concentration was determined using the Pierce BCA (bicinchoninic acid) method. The values of the cellular uptake were normalized to the percentage of the total amount of radioactivity added, corresponding to an inject dose per 100 μg protein (%ID/100 μg protein).

Real-Time Polymerase Chain Reaction

The total RNA was extracted from cells using Trizol reagent (cat no. 9109; Takara, Liaoning, China) following by the manufacturer's instructions. Briefly, 1 μg of each RNA sample was reverse transcribed to generate the cDNA using the PrimeScript RT Master Mix kit (cat no. RR036A; Takara). Quantitative real-time PCR was performed using the SYBR Premix Ex Taq TM kit (cat no. RR420A; Takara) with an ABI PRISM 7500 Real-time PCR System (Applied

Biosystems, Foster, CA, USA). The sequences of the primers (synthesized by Sangon Biotech) for the target RNA were Fwd 5′-CTTGATCCTGGCTGTGGACT-3′ and Rev 5′-GCTCTGTGCTTCTCGACTCC-3′. The amount of ASCT2 was normalized to the amount of GAPDH cDNA (cat no. B661104; Sangon Biotech, Shanghai, China).

Western Blot

The cells and tumor tissue were lysed with tissue proteins and extracted with RIPA buffer. The protein concentration was measured using the BCA protein assay kit (Pierce Chemical, Rockford, IL, USA). After that, 20–40 μg of total protein extracts from each sample was separated on 8 % gradient SDS-polyacrylamide gels (Invitrogen) and transferred to PVDF membranes (Pierce Chemical). The membranes were blocked for 2 h at room temperature with 5 % non-fat milk blocking buffer and incubated with anti-ASCT2 (Abcom, ab58690, 1:400 diluted), anti-*MYCN* (Proteintech, 10159, 1:500), and anti-LAT1 (Affinity Biosciences, DF8065, 1:1000) overnight at 4 °C. The membranes were washed 3 times with TBST prior to incubation with an anti-species HRP-conjugated antibody (1:1000; Santa Cruz Biotechnology) for 1 h at room temperature. Mouse anti-GAPDH (cat no. AG019; Beyotime, China, 1:1000 diluted) was invoked as a loading control. After washing 3 times, the membrane was imaged with BIO-RAD Gel Doc XR+. The images were opened and analyzed by ImageLab (BIO-RAD) software. Samples of each tumor models were prepared for the western blot to obtain semiquantitative data for statistical analysis.

Immunofluorescence

The tumor sections were fixed in 4 % formalin, embedded in paraffin, and incubated in buffered normal goat serum for 1 h at room temperature to prevent nonspecific binding of the antibodies. Then, the tumor sections were incubated separately overnight with antibodies purchased from Sigma against ASCT2 (cat no. HPA035240; dilution 1:100), Servicebio against Ki-67 (cat no. GB13030-2; dilution 1:200), and Abcam against c-Caspase 3 (cat no. Ab199963; dilution 1:300), and then followed by incubation with Cy3 goat anti-rabbit IgG (cat no. GB21303; dilution 1:300; Servicebio) and Alexa Fluor 488 goat anti-rat IgG (cat no. GB25303; dilution 1:400; Servicebio) for 1 h at 37 °C. Thereafter, the sections were washed in PBS. 4′,6-Diamidino-2-phenylindole (DAPI) was utilized to stain the cell nuclei (blue) (cat no. G1012; Servicebio). Photomicrographs were taken with a DMI3000B camera (Leica).

ASCT2 shRNA Knockdown

Stable ASCT2 knockdown was achieved by infection with lentivirus, using the pleno-gph-puro vector containing an ASCT2-specific short hairpin RNA (shASCT2; GCTGCTTATCCGCTTCTTCAA; Biolink, Shanghai). The control plasmid consisted of a plant microRNA sequence (shControl; TTCTCCGAACGTGTCACGT; Biolink, Shanghai), which has no specific targets in mammalian cells as previously detailed [20]. The infected cells were enriched by puromycin (10 μg/ml) selection, and protein knockdown was confirmed by RT-PCR and WB.

Animal Models

All animal studies were performed in accordance with the Chinese Guidelines for Animal Care and Ethic for Animal Experiments, and the experimental protocols were approved by the institutional guidelines for the care and use of animals. Female BALB/c nude mice were purchased from Shanghai Slack Experimental Animal Center of qualified animals SCXK, at 4–6 weeks of age and mean weight 20–22 g. SH-SY5Y, SK-N-BE (2), and IMR-32 cells were grown in log-phase for 24 h. A total number of 1×10^7 cells of IMR-32, SK-N-BE (2), and IMR-32 (shControl or shASCT2) cell lines and 5×10^6 of the SH-SY5Y cell line were injected subcutaneously in the right or left shoulder of female BALB/c nude mice with matrigel (serum-free DMEM:matrigel = 1:1). The mice were then examined weekly for any sign of tumorigenic growth. PET/CT imaging was performed when the tumor volume was at least 200 mm^3 (6–8 weeks after inoculation).

Biodistribution

For biodistribution, the BALB/c nude mice ($n = 4$ each time point) and neuroblastoma tumor models ($n = 3$ each time point) were injected intravenously with 15 MBq of 4-[^{18}F]FGln *via* the tail vein and sacrificed at selected time points (5 min, 15 min, 30 min, 45 min, 60 min, and 120 min) under isoflurane anesthesia. Mouse blood samples were obtained from the retro-orbital venous plexus, the organs of interest (brain, heart, lung, liver, intestine, kidney, muscle, and kidney), and tumors were harvested and weighed, and the activity contained therein was counted in a γ-counter. The injected dose per gram of tissue was calculated from the organ weight and counted activities, based on the individually administered doses.

PET/CT Imaging of Mouse Models

PET/CT was performed with BALB/c mouse modes ($n = 14$) using the small animal PET/CT scanner-micro (SNPC-103, Pingseng, China). Prior to imaging, each group xenografts (IMR-32 tumors ($n = 4$), SK-N-BE (2) tumors ($n = 4$), and SH-SY5Y tumors ($n = 6$)) were fasted 6–8 h for [^{18}F]FDG PET/CT imaging and 4-[^{18}F]FGln imaging. The mice were administered approximately 200 μl of PET imaging agent at 7.4–10.8 MBq *via* intravenous injection and were allowed

free access to water and kept in a 30 °C warmed chamber during the uptake period. Subsequently, the animals were anesthetized through inhalation with 3 % isoflurane and maintained with 1.5 % isoflurane with 40 % oxygen and 60 % nitrogen (gas flow 1 l/min). Dynamic small-animal PET scan were conducted with 4-[^{18}F]FGln in SH-SY5Y cell, SK-N-BE (2) cell, and IMR-32 cell mouse models for 120 min. Ten minutes of static data of 4-[^{18}F]FGln and [^{18}F]FDG PET/CT imaging were recorded at 20–30 min, 50–60 min, and 110–120 min after injection. The two PET imaging were performed in the same animal models within 3 days. Animals were positioned in a prone position with their medial axis parallel to the axial axis of the PET scanner and into the center of the field of view. PET data were reconstructed using the Avatar software to draw regions of interest (ROI) surrounding the entire tumor volume and the observed maximum pixel value was represented as the maximum standardized uptake value (SUVmax). Tumor (SUVmax)-to-muscle (SUVmean) (T/M) ratios were determined by normalizing tumor uptake to muscle uptake.

Targeting ASCT2 Attenuates Tumor Growth In Vivo

The stable ASCT2 knockdown (KD) cell line clones using lentiviral shRNA against human ASCT2 (ASCT2-KD) and nonspecific shRNA control (negative control) were generated in IMR-32 cells. We injected stable lines of either ASCT2-KD (shASCT2-IMR-32) or negative control (shControl-IMR-32) cells subcutaneously into the flank of nude mice ($n = 4$, each group). The size of the tumor was evaluated twice a week with a caliper, and the tumor volume (cm^3) was calculated using the following formula: $V = (\text{length} \times \text{width}^2)/2$. The mice were imaged, as described previously. The mice were euthanized after imaging, and the tumors were isolated, photographed, measured, and weighted.

Statistical Analysis

In vitro, all the experiments were similarly conducted twice. Experimental replicates of %ID/μg, SUV and percent change in volume are presented as the mean ± standard deviation, unless otherwise noted. One-way ANOVA and nonparametric tests were used to examine the statistical significance of cell uptake of neuroblastomas in the *in vitro* datasets. For *in vivo* data analysis, the tumor-to-muscle ratio comparisons in xenograft tumor models were evaluated using *t* tests, one-way ANOVA, two-way ANOVA, and nonparametric tests. Analysis of relative gene expression data using real-time quantitative PCR and the $2^{-\Delta\Delta CT}$ method. Data analyses and graphs were conducted and plotted using the GraphPad Prism 6.0 software package and SPSS, version 20.0 (IBM Corp, Armonk, NY, USA). Comparisons were considered statistically significant if the *P* values were lower than 0.05.

Results

In Vitro Uptake of 4-[^{18}F]FGln in Cell Lines

The time-dependent uptake of 4-[^{18}F]FGln and [^{18}F]FDG was determined in *MYCN*-amplified cells (SH-SY5Y cells, IMR-32 cells) and non-*MYCN*-amplified cells (SK-N-BE (2) cells) and is shown in Fig. 1a. Our results show a high uptake of 4-[^{18}F]FGln in *MYCN*-amplified cell lines, and the uptake of IMR-32 cells was also higher than that of SK-N-BE (2) cell at different time points ($P < 0.05$). Significant uptake of 4-[^{18}F]FGln in IMR-32 cells and SK-N-BE (2) cells was observed at 15 min of incubation, reaching a maximum of 31.6 ± 1.7 and 21.6 ± 6.6 %ID per 100 μg of protein at 60 min. Longer incubation did not increase the cellular uptake of 4-[^{18}F]FGln, which was up to 30.9 ± 1.5 and 20.1 ± 1.1 %ID per 100 μg of protein at 120 min, respectively. The non-*MYCN*-amplified cells showed different 4-[^{18}F]FGln uptake kinetics, reaching the maximum at 60 min (16.9 ± 1.4 %ID per 100 μg of protein), and decreasing quickly. The IMR-32 cells and SK-N-BE (2) cells showed 1.8-fold and 1.2-fold increase in 4-[^{18}F]FGln uptake at 60 min compared with SH-SY5Y cell, respectively (IMR-32 *vs* SH-SY5Y, $P < 0.001$; SK-N-BE (2) *vs* SH-SY5Y, $P < 0.001$).

As shown in Fig. 1b, there was no significant difference in the FDG uptake between the *MYCN*-amplified cell lines and the non-*MYCN*-amplified cell lines at 15 min, 30 min, and 60 min. When reaching 120 min, the uptake of SH-SY5Y cells was significantly higher than that of IMR-32 cells ($P = 0.022$).

In Vivo Studies

Biodistribution of 4-[^{18}F]FGln in BALB/c Nude Mice In vivo, the biodistribution of 4-[^{18}F]FGln was performed on BALB/c nude mice, which is a well-known and established animal model. The mice ($n = 3$ per group) were injected I.V. with 7.4 MBq (200 μCi) of 4-[^{18}F]FGln and sacrificed at selected time points (5 min, 15 min, 30 min, 45 min, 60 min, and 120 min) under isoflurane anesthesia. The organs of interest and blood were measured after injection. The results of the biodistribution experiment in mice are presented in Table 1. It shows the expected behavior of a significant uptake in the intestines (7.46, 6.13, 6.30, and 6.42 %ID/g at 5 min, 45 min, 60 min, and 120 min), most likely due to the radiolabeled amino acid excreted through the gastrointestinal tract. The levels in the blood and heart dropped quickly with time, reaching 7.89 and 8.76 %ID/g at 5 min and showing a low uptake at 120 min after injection (2.89 and 2.71 %ID/g). 4-[^{18}F]FGln showed a moderate liver uptake with relatively slow washout rate. Rapid uptake was observed within the kidneys, with a peak of 7.54 %ID/g at 30 min but was quickly excreted through the urinary bladder, reaching 2.32 %ID/g at 120 min. The brain exhibited a relatively

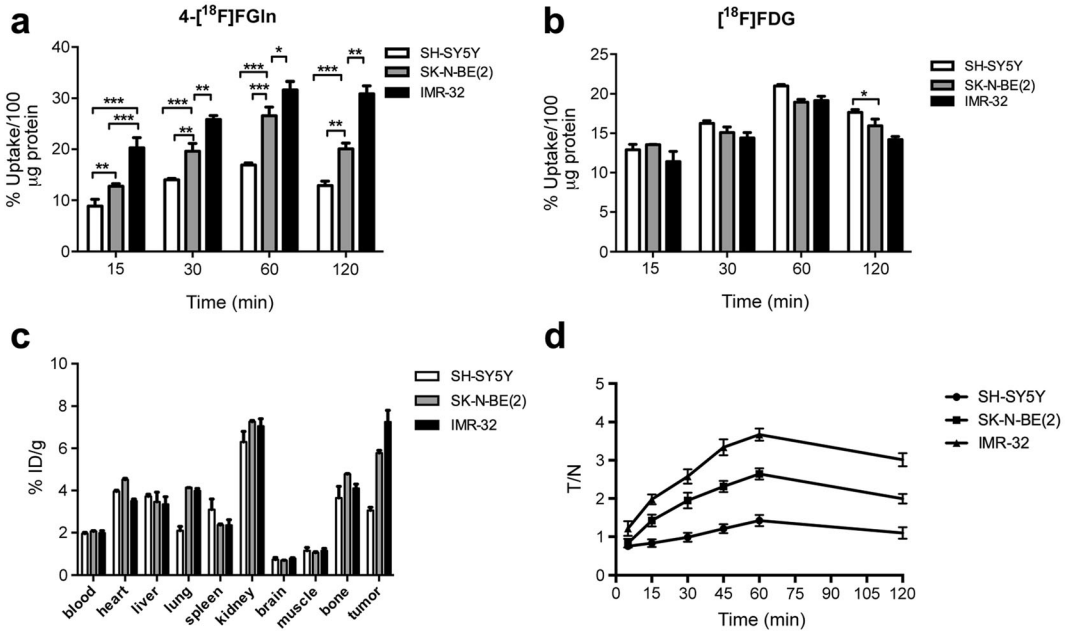

Fig. 1. The neuroblastoma tumors of IMR-32 and SK-N-BE (2) show relative higher uptake than SH-SY5Y. **a** The uptake of 4-[18F]FGln showing in three neuroblastoma cell lines that the maximum uptake of neuroblastoma cells reaching at 60 min. **b** [18F]FDG uptake showing in three neuroblastoma cell lines over incubation time. **c***In vivo* biodistribution of approximately 15 MBq 4-[18F]FGln in neuroblastoma tumor-bearing nude mice at 60 min after injection, columns mean %ID/g ($n = 3$ per group). **d** Time-activity curve (TAC) for 4-[18F]FGln after intravenous injection into BALB/c nude mice ($n = 3$ each group) bearing neuroblastoma tumor on small-animal PET/CT; T/M = tumor(SUVmax)/muscle(SUVmean).

low but consistent uptake. The bone showed a rapid uptake and dropped with time, remaining at 3.67 %ID/g at 120 min after injection.

In Vivo Biodistribution in Mice Models The time-dependent biodistribution studies were performed in SH-SY5Y, SK-N-BE (2), and IMR-32 xenografted BALB/c mice (Fig. 1c). The results of our study exhibited the highest uptake of 4-[18F]FGln in tumors at 60 min, compared with that in non-tumor tissue. The uptake of 4-[18F]FGln in *MYCN*-amplified tumors reached 6.6 ± 0.3 %ID/g (IMR-32) and 5.6 ± 0.2 %ID/g (SK-N-BE (2)) at 60 min after injection. However, in the non-*MYCN*-amplified tumor, the uptake was 3.7 ± 0.1 %ID/g (SH-SY5Y). Bone uptake (femur) remained at 5.0–6.0 %ID/g at 60 min after injection, implying that defluorination of the compound may be occurring *in vivo*. The uptake of the kidney was as high as the *MYCN*-amplified tumors, due to the radiolabeled agent partly remaining in the urinary system. The tumor-to-muscle ratio (T/M) after injection is shown in Fig. 1d. The tumors showed an increasing uptake until reached 60 min and then slightly dropped at 120 min. Of the three tumors, the IMR-32 showed the highest uptake.

4-[18F]FGln PET/CT Imaging in NB Xenograft Models To explore the potential of 4-[18F]FGln PET imaging in NB

Table 1. *In Vivo* biodistribution of 4-[18F]FGln in BALB/c nude mice after intravenous injection

Organ	5 min	15 min	30 min	45 min	60 min	120 min
Heart	8.76 ± 0.25	5.23 ± 0.30	4.80 ± 0.20	3.80 ± 0.20	3.53 ± 0.30	2.89 ± 0.23
Blood	7.89 ± 0.36	5.43 ± 0.42	4.32 ± 0.56	3.21 ± 0.33	2.98 ± 0.36	2.71 ± 0.24
Lung	5.73 ± 0.60	3.66 ± 0.15	3.03 ± 0.21	2.73 ± 0.21	2.46 ± 0.27	2.12 ± 0.17
Liver	8.26 ± 0.21	7.20 ± 0.20	6.11 ± 0.45	5.10 ± 0.30	4.63 ± 0.35	3.78 ± 0.31
Intestines	7.46 ± 0.30	6.30 ± 0.20	5.80 ± 0.20	6.13 ± 0.42	6.30 ± 0.41	6.42 ± 1.12
Muscle	2.63 ± 0.21	3.26 ± 0.21	2.90 ± 0.20	3.11 ± 0.36	2.72 ± 0.11	2.13 ± 0.24
Bone	6.33 ± 0.40	5.20 ± 0.11	4.53 ± 0.25	4.1 ± 0.20	4.13 ± 0.30	3.67 ± 0.89
Kidney	3.13 ± 0.25	5.91 ± 0.23	7.45 ± 0.62	5.14 ± 0.47	3.23 ± 0.45	2.32 ± 0.14
Brain	1.50 ± 0.03	1.3 ± 0.01	1.20 ± 0.10	1.20 ± 0.10	1.20 ± 0.12	1.15 ± 0.08

Data represented as %ID/g, mean ± SD ($n = 4$ mice per time point)

xenograft models, we evaluated tracer accumulation at 30 min, 60 min, and 120 min in xenograft tumors. Based on the T/M ratio in IMR-32 and SK-N-BE (2), the uptake ratios of the tumors were 2.24 and 2.05 at 30 min, reaching to a ratio of 3.71 and 2.63 at 60 min and then decreasing to 3.10 and 2.15 at 120 min after injection, respectively. By contrast, the T/M ratios of 4-[^{18}F]FGln in SH-SY5Y tumors were 1.10, 1.54, and 1.23 at 30, 60, and 120 min, respectively. The maximum uptake of 4-[^{18}F]FGln in IMR-32 and SK-N-BE (2) tumors was significantly higher than that in SH-SY5Y tumor ($P < 0.001$). In comparison to 4-[^{18}F]FGln, the T/M ratio of [^{18}F]FDG was 1.90, 1.21, and 1.23 in IMR-32, SK-N-BE (2), and SH-SY5Y at 60 min, respectively. The uptake of 4-[^{18}F]FGln in the IMR-32 tumor and SK-N-BE (2) tumor was 2.3-fold and 2.1-fold higher than that of [^{18}F]FDG at 60 min, respectively (Fig. 2).

ASCT2 Expression in MYCN-Amplified Neuroblastoma Tissues and Cells To understand whether the expression of ASCT2 influenced the 4-[^{18}F]FGln uptake in three neuroblastoma cell lines, we evaluated the ASCT2 level in neuroblastoma cells and tumor tissues using IF and WB. The *MYCN* expressions of three tumors are shown in Fig. 3a–d. *MYCN* is differentially expressed in IMR-32, SK-N-BE (2), and SH-SY5Y tissues and cell lines ($P < 0.001$). ASCT2 protein was overexpressed in *MYCN*-amplified neuroblastoma tissues and cells (IMR-32 and SK-N-BE (2)) compared with non-*MYCN*-amplified neuroblastoma (SH-SY5Y).

ASCT2 Knockdown In Vivo Represses MYCN-Amplified Neuroblastoma Growth and Uptake of 4-[^{18}F]FGln To determine whether ASCT2 is directly responsible for tumor growth and uptake of 4-[^{18}F]FGln, we knocked down ASCT2 expression in IMR-32 cells and SK-N-BE (2) cells using a lentiviral shRNA vector. Stable antibiotic selection of shASCT2-expressing cells was only successful in IMR-32 cells as SK-N-BE (2) cells died rapidly after transduction. In the *in vitro* studies (Fig. 4a), the cell uptake of 4-[^{18}F]FGln in shASCT2-IMR-32 was 2.1-fold lower than that of ShControl-IMR-32 at 60 min, indicating that the ASCT2 knockdown markedly attenuated the ability of IMR-32 to utilize glutamine. No significant difference in [^{18}F]FDG uptake was observed between shASCT2-IMR-32 cell and shControl-IMR-32 cells.

ASCT2 knockdown was confirmed in IMR-32 cells by relative quantification of mRNA and western blotting (Fig. 4b). The expression of LAT1 in shASCT2 cells was mildly upregulated, and there were no significant differences between the shControl and shASCT2 cells (Fig. 4c).

Subsequently, IMR-32 cells expressing shControl or shASCT2 were subcutaneously injected into nude mice and the shASCT2 tumor was monitored twice a week until the tumor size was significant.

In the *in vivo* study, neuroblastoma xenografts bearing shASCT2-IMR-32 showed a significant decrease in 4-[^{18}F]FGln uptake on PET/CT, while shControl mouse models exhibited a sharp uptake of 4-[^{18}F]FGln (Fig. 4d). The expression of ASCT2 was reduced in shASCT2 tumors compared with shControl tumors, while the LAT1 level showed no significant difference between shASCT2 tumors and shControl (Fig. 4c).

The volume of shControl tumors was significantly larger than shASCT2 tumors ($P < 0.05$). The weight of the shControl tumors was 1.2-fold than that of shASCT2 tumors ($P < 0.05$) (Fig. 5a). Ki-67 expression (the proliferation

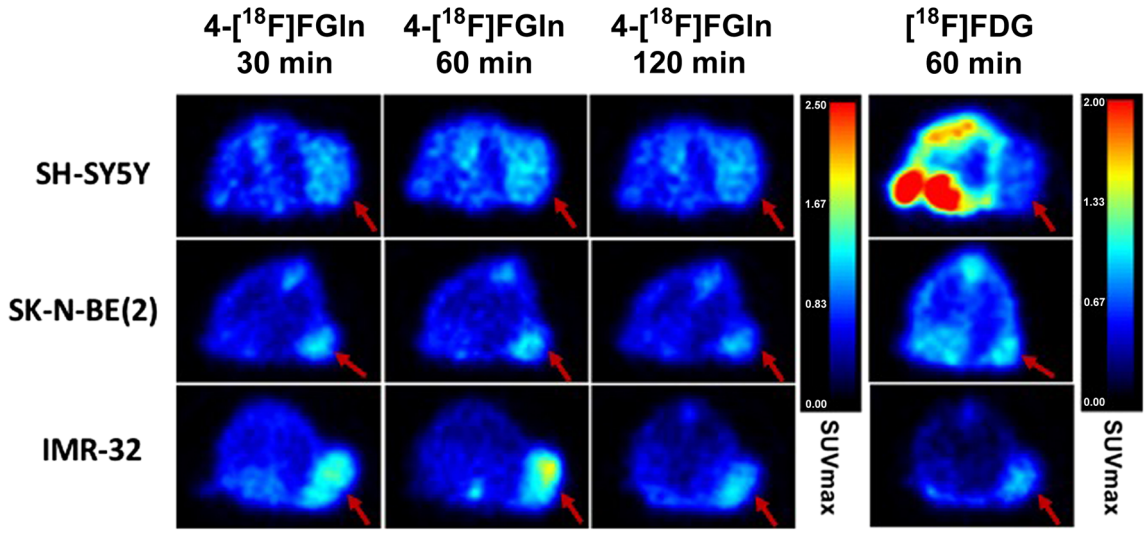

Fig. 2. 4-[^{18}F]FGln shows high uptake in *MYCN*-amplified xenografts but low uptake in non-*MYCN*-amplified xenografts. Comparison of 4-[^{18}F]FGln and [^{18}F]FDG uptake at 0.5, 1, and 2 h after injection in IMR-32 tumors ($n = 4$), SK-N-BE (2) tumors ($n = 4$), and SH-SY5Y tumors ($n = 6$).

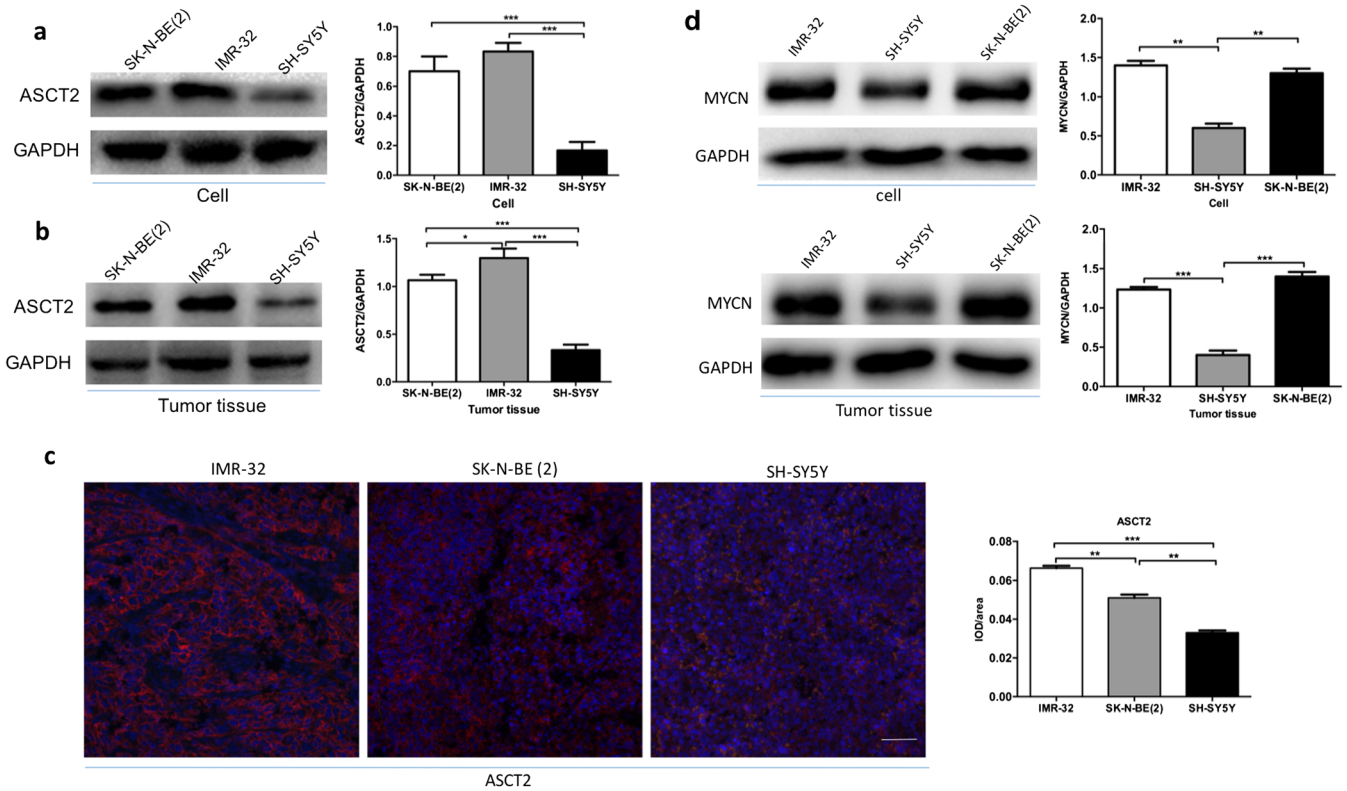

Fig. 3. Overexpression of ASCT2 is showed in *MYCN*-amplified neuroblastoma cells and tumors. **a** ASCT2 overexpressed in IMR-32 and SK-N-BE (2) cell lines. **b** ASCT2 overexpressed in IMR-32 and SK-N-BE (2) xenograft tumors. **c** IF analysis showed the higher expression of ASCT2 in IMR-32 and SK-N-BE (2) bearing xenograft tumors than that in SH-SY5Y. Scale bar = 50 μm. **d** MYCN overexpressed in IMR-32 and SK-N-BE (2) cells and tumors. * $P < 0.05$; ** $P < 0.01$; *** $P < 0.001$.

biomarker) of xenograft tumors was consistently lower in the shASCT2 tumors while cleaved caspase-3 (c-Caspase3) level was higher compared with shControl tumors (Fig. 5b).

Discussion

Glutamine addiction plays an important role in specific metabolic adaptation and has been reported in many cancer cells [21–24]. In this study, we attempted to evaluate the diagnosis and target therapeutic value of 4-[18F]FGln PET in *MYCN*-amplified neuroblastoma. Previously studies have demonstrated that *MYCN*-amplified neuroblastoma exclusively rely on large amounts of exogenous glutamine to maintain sufficient levels of glutamine essential for the TCA cycle anaplerosis and cell viability [12, 13, 25]. In this study, our results showed that *MYCN*-amplified neuroblastoma had greater 4-[18F]FGln uptake to maintain the abnormal proliferation and growth than non-*MYCN*-amplified neuroblastoma, which may provide the ability for 4-[18F]FGln PET imaging to distinguishing the genetic typing of neuroblastoma. *MYCN*-amplified is one of the unfavorable prognostic features and influences the risk stratification of pediatric patients with neuroblastoma. The status of *MYCN*-amplication is closely linked to the therapeutic outcome of neuroblastoma. 4-[18F]FGln PET imaging as a non-invasive examination seems likely to provide some useful information to guide the therapy in the future.

In order to develop glutamine PET imaging agents, the preparation of a 5-[11C]-(2s)-glutamine ([11C]Gln) simple program has already been reported, due to fact that the half-life of F-18 (110 min) is 5.5 times that of C-11 (20 min); therefore, F-18 labeling tracer is more suitable for further fields of preparation and transportation. Only natural L-glutamine derivatives of 4-[18F]FGln and 4-[18F]FGln showed a significant uptake and continuous uptake in tumor cells. A recent study showed that the uptake of 4-[18F]FGln in xenograft tumors is related to the levels of ASCT2 [16]. In the *in vitro* studies, the uptake of 4-[18F]FGln in SH-SY5Y cell was 1.87-fold and 1.27-fold lower than that in IMR-32 cell and SK-N-BE (2) cell. In the *in vivo* PET/CT imaging of mice models, 4-[18F]FGln exhibited a high uptake and long retention in the *MYCN*-amplified neuroblastoma xenografted tumors, and the maximum uptake time in neuroblastoma tumor was around 60 min. However, [18F]FDG showed a moderate uptake in cells and tumors of neuroblastoma mouse models, and the T/M ratio in the *in vivo* study was much lower than 4-[18F]FGln in the uniform model. In addition, our results also showed that the

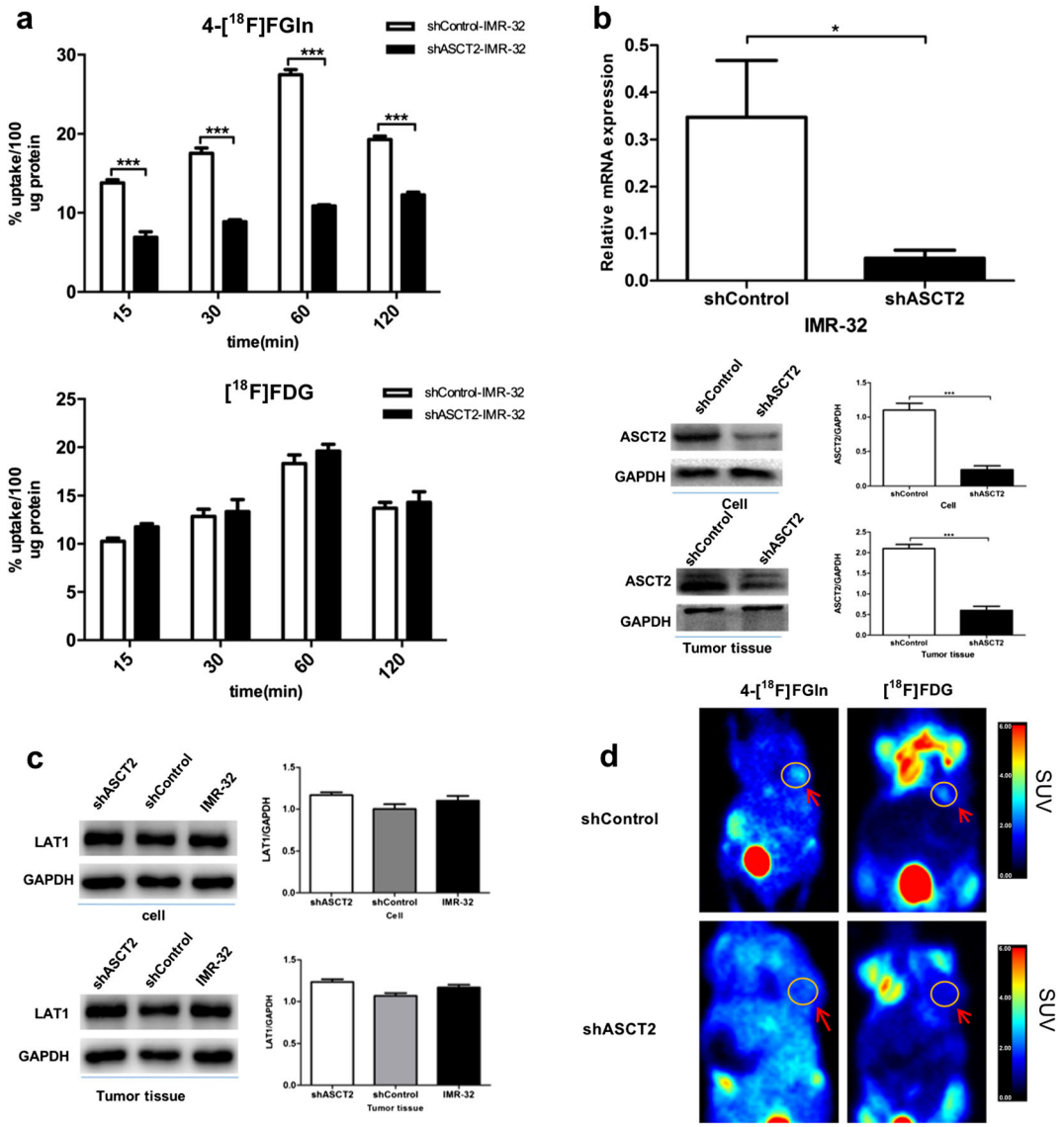

Fig. 4. The uptake of 4-[18F]FGln reduced in *ASCT2* knockdown tumors and cells and analysis of ASCT2 and LAT1 proteins after shRNA knockdown. **a** 4-[18F]FGln uptake in shASCT2-IMR-32 showed lower uptake than that in shControl-IMR-32, while [18F]FDG uptake showed no significant difference during the 120 min. **b** Relative mRNA expression of ASCT2 was calculated by $2^{-\Delta\Delta Ct}$ method, and a reduced expression was observed after shASCT2 knockdown; ASCT2 expression showed a significant difference between in shASCT2 and shControl cells and tumor tissues. **c***ASCT2* knockdown had no significant effect on the expression of LAT1 protein. **d** 4-[18F]FGln and [18F]FDG PET imaging showed low uptake in IMR-32 tumor after *ASCT2* knockdown. $n = 3$ for each time point; significance was assessed using nonparametric test; $^{*}P < 0.05$; $^{**}P < 0.01$; $^{***}P < 0.001$.

uptake of 4-[18F]FGln reached a maximum around 60 min and then decreased in neuroblastoma cell lines, which was different from some other cells as reported, such as 9L cells [14] and MCF-7 cells [26], due to different kinetics of the cells.

MYC oncogenes regulate multiple aspects of tumor metabolism, enabling cancer cells to avidly take up both Glc and Gln [27]. In our study, *in vivo* and *in vitro* results found that there was no significant difference between *MYCN*-amplified neuroblastoma and non-*MYCN*-amplified neuroblastoma in FDG uptake. Nevertheless, the study by Liu et al. [28] demonstrated that NB with *MYCN* amplification in patients was correlated with a higher FDG uptake. The reason for this be that SH-SY5Y cells are controlled by *ALK*, which requires a large amount of glucose to maintain metabolism and growth [29], which leads to a high uptake of [18F]FDG in SH-SY5Y cells and tumors. As a measure for metabolic glucose tracer, [18F]FDG has limitations in neuroblastoma because of the prominent uptake both in inflammation and tumors. Therefore, our results suggested that 4-[18F]FGln as a novel imaging agent exhibited high uptake in *MYCN*-amplified neuroblastoma cells and mouse

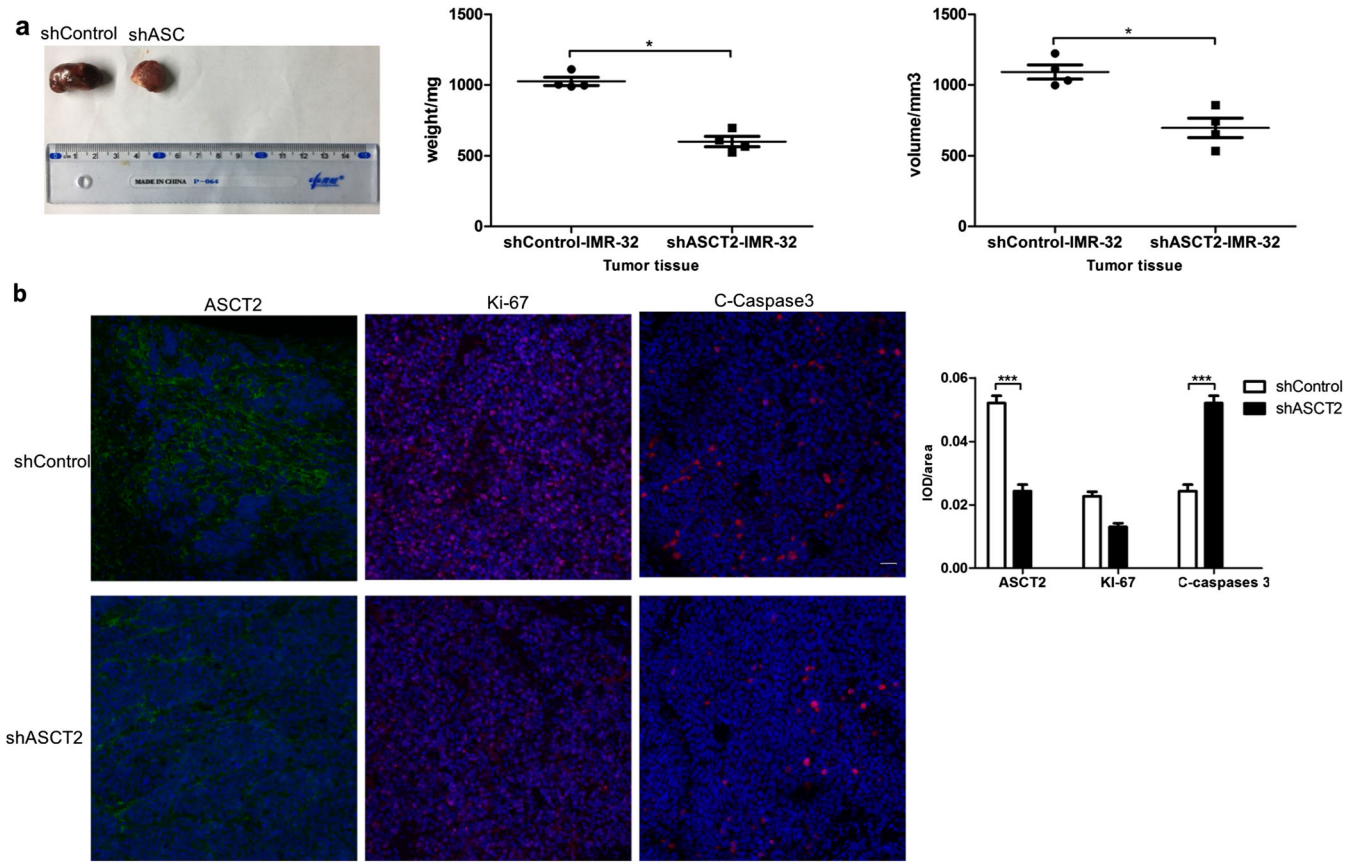

Fig. 5. ASCT2 slows the growth after ASCT2 knockdown in IMR-32 neuroblastoma. **a** Tumor growth (volume and weight) was measured after 8 weeks in shControl ($n = 4$) and shASCT2 ($n = 4$) mice. **b** Expression levels of ASCT2 and Ki-67 were low and c-Caspase3 was highly expressed in shASCT2 tumors. Scale bar = 50 μm; significance was assessed using nonparametric test; $^{*}P < 0.05$; $^{**}P < 0.01$; $^{***}P < 0.001$.

models, and 4-[18F]FGln PET imaging may provide further evidence for the diagnosis of *MYCN*-amplified neuroblastoma.

4-[18F]FGln uptake is mainly mediated by the amino acid transporter ASCT2 [14, 30], which is markedly increased in *MYCN*-amplified neuroblastoma. As shown in this study, ASCT2 is high overexpressed in IMR-32 and SK-N-BE (2) cells and tumors of neuroblastoma xenografts compared with SH-SY5Y; and the higher the ASCT2 expression level, the higher is the 4-[18F]FGln uptake. Notably, amplification of the *MYCN* gene in neuroblastoma is associated with an aggressive phenotype [31] and poor prognosis, which makes the subsequent therapy of neuroblastoma patients a medical challenge. *MYCN*-amplified neuroblastomas are frequently resistant to conventional therapeutic drugs, due in part to defects in death-inducing signaling complex (DISC) components. In a previous study, Ren et al. [13] studied a large number of primary neuroblastoma tumors and reported that ASCT2 overexpression may be related to poor prognosis in neuroblastomas. Shimizu et al. [32] also identified ASCT2 as a potential marker for prognosis in non-small cell lung cancer. These findings provide a strong rationale for developing highly specific small-molecule inhibitors or monoclonal antibodies against ASCT2 in treating *MYCN*-amplified neuroblastoma that are resistant to routine chemotherapy. Our results showed that the uptake of 4-[18F]FGln decreased in the shRNA-mediated knock down of ASCT2 in *MYCN*-amplified cell lines and mouse models, corresponding to a decrease in tumor volume in the knockdown of ASCT2 mouse models. This suggests that ASCT2-targeted therapies may be particularly helpful in *MYCN*-amplified neuroblastoma.

The limitations of this study include a limited number of neuroblastoma cell lines and reliance on the primary static imaging uptake measures. Future studies should examine a wider range of neuroblastoma subtypes as well as other glutaminolytic cancers and validate tumor with kinetic analysis of 4-[18F]FGln uptake.

Conclusion

In summary, 4-[18F]FGln PET imaging serves as a valuable tool in imaging *MYCN*-amplified neuroblastoma. ASCT2 is the major glutamine transporter that regulates metabolism and may be a therapy target for *MYCN*-amplified neuroblastoma.

Acknowledgements. All authors thank the Institutional Technology Service Center of Shanghai Institute of Materia Medica for the technical support.

Authors' Contributions. CL and RH supervised the process of the study and performed the manuscript writing. HS, ZH, and CW performed the xenograft mice study and PET imaging. JG and LS are responsible for the radiolabeling of 4-[^{18}F]FGln and [^{18}F]FDG. CL and SH participated in western blot, real-time PCR work and IF. LL, CL, and LS are responsible for the data analysis. HW as scientific director has coordinated and approved the work. All authors read and approved the final manuscript.

Funding. This work was supported by the National Natural Science Foundation (91859106, 81771890), the "Personalized Medicines—Molecular Signature-based Drug Discovery and Development," Strategic Priority Research Program of the Chinese Academy of Sciences (XDA12020108), and One Hundred Talent Program of Chinese Academy of Sciences.

Compliance with Ethical Standards

Conflict of Interest

The authors declare that they have no conflict of interest.

Ethics Approval

All applicable international, national, and institutional guidelines for the care and use of animals were followed.

Publisher's Note. Springer Nature remains neutral with regard to jurisdictional claims in published maps and institutional affiliations.

References

1. Luksch R, Castellani MR, Collini P, de Bernardi B, Conte M, Gambini C, Gandola L, Garaventa A, Biasoni D, Podda M, Sementa AR, Gatta G, Tonini GP (2016) Neuroblastoma (peripheral neuroblastic tumours). Crit Rev Oncol Hematol 107:163–181
2. Huang M, Weiss WA (2013) Neuroblastoma and MYCN. Cold Spring Harb Perspect Med 3:a014415
3. Yuneva M, Zamboni N, Oefner P, Sachidanandam R, Lazebnik Y (2007) Deficiency in glutamine but not glucose induces MYC-dependent apoptosis in human cells. J Cell Biol 178:93–105
4. Broer A, Rahimi F, Broer S (2016) Deletion of amino acid transporter ASCT2 (SLC1A5) reveals an essential role for transporters SNAT1 (SLC38A1) and SNAT2 (SLC38A2) to sustain glutaminolysis in cancer cells. J Biol Chem 291:13194–13205
5. Fuchs BC, Bode BP (2005) Amino acid transporters ASCT2 and LAT1 in cancer: partners in crime? Semin Cancer Biol 15:254–266
6. Janpipatkul K, Suksen K, Borwornpinyo S, Jearawiriyapaisarn N, Hongeng S, Piyachaturawat P, Chairoungdua A (2014) Downregulation of LAT1 expression suppresses cholangiocarcinoma cell invasion and migration. Cell Signal 26:1668–1679
7. Wasa M, Wang HS, Okada A (2002) Characterization of L-glutamine transport by a human neuroblastoma cell line. Am J Physiol Cell Physiol 282:C1246–C1253
8. Nicklin P, Bergman P, Zhang B, Triantafellow E, Wang H, Nyfeler B, Yang H, Hild M, Kung C, Wilson C, Myer VE, MacKeigan JP, Porter JA, Wang YK, Cantley LC, Finan PM, Murphy LO (2009) Bidirectional transport of amino acids regulates mTOR and autophagy. Cell 136:521–534
9. Boroughs LK, DeBerardinis RJ (2015) Metabolic pathways promoting cancer cell survival and growth. Nat Cell Biol 17:351–359
10. Wise DR, DeBerardinis RJ, Mancuso A, et al. (2008) Myc regulates a transcriptional program that stimulates mitochondrial glutaminolysis and leads to glutamine addiction. Proc Natl Acad Sci U S A 105:18782–18787
11. Gao P, Tchernyshyov I, Chang TC, Lee YS, Kita K, Ochi T, Zeller KI, de Marzo AM, van Eyk JE, Mendell JT, Dang CV (2009) c-Myc suppression of miR-23a/b enhances mitochondrial glutaminase expression and glutamine metabolism. Nature 458:762–765
12. Qing G, Li B, Vu A, Skuli N, Walton ZE, Liu X, Mayes PA, Wise DR, Thompson CB, Maris JM, Hogarty MD, Simon MC (2012) ATF4 regulates MYC-mediated neuroblastoma cell death upon glutamine deprivation. Cancer Cell 22:631–644
13. Ren P, Yue M, Xiao D, Xiu R, Gan L, Liu H, Qing G (2015) ATF4 and N-Myc coordinate glutamine metabolism in MYCN amplified neuroblastoma cells through ASCT2 activation. J Pathol 235:90–100
14. Lieberman BP, Ploessl K, Wang L, Qu W, Zha Z, Wise DR, Chodosh LA, Belka G, Thompson CB, Kung HF (2011) PET imaging of glutaminolysis in tumors by ^{18}F-(2S,4R)4-fluoroglutamine. J Nucl Med 52:1947–1955
15. Qu W, Zha Z, Ploessl K, Lieberman BP, Zhu L, Wise DR, B. Thompson C, Kung HF (2011) Synthesis of optically pure 4-fluoroglutamines as potential metabolic imaging agents for tumors. J Am Chem Soc 133:1122–1133
16. Hassanein M, Hight MR, Buck JR, Tantawy MN, Nickels ML, Hoeksema MD, Harris BK, Boyd K, Massion PP, Manning HC (2016) Preclinical evaluation of 4-[^{18}F]fluoroglutamine PET to assess ASCT2 expression in lung Cancer. Mol Imaging Biol 18:18–23
17. Schulte ML, Hight MR, Ayers GD, Liu Q, Shyr Y, Washington MK, Manning HC (2017) Non-invasive glutamine PET reflects pharmacological inhibition of BRAFV600E in vivo. Mol Imaging Biol 19:421–428
18. Venneti S, Dunphy MP, Zhang H et al (2015) Glutamine-based PET imaging facilitates enhanced metabolic evaluation of gliomas in vivo. Sci Transl Med 7:274ra217
19. Zhu L, Ploessl K, Zhou R, Mankoff D, Kung HF (2017) Metabolic imaging of glutamine in cancer. J Nucl Med 58:533–537
20. Choi YJ, Hwang HS, Kim HJ, Jeong YH, Cho A, Lee JH, Yun M, Lee JD, Kang WJ (2014) ^{18}F-FDG PET as a single imaging modality in pediatric neuroblastoma: comparison with abdomen CT and bone scintigraphy. Ann Nucl Med 28:304–313
21. Wise DR, Thompson CB (2010) Glutamine addiction: a new therapeutic target in cancer. Trends Biochem Sci 35:427–433
22. Csibi A, Fendt SM, Li C, Poulogiannis G, Choo AY, Chapski DJ, Jeong SM, Dempsey JM, Parkhitko A, Morrison T, Henske EP, Haigis MC, Cantley LC, Stephanopoulos G, Yu J, Blenis J (2013) The mTORC1 pathway stimulates glutamine metabolism and cell proliferation by repressing SIRT4. Cell 153:840–854
23. Marquez J, Alonso FJ, Mates JM et al (2017) Glutamine addiction in gliomas. Neurochem Res 42:1735–1746
24. Choi YK, Park KG (2018) Targeting glutamine metabolism for cancer treatment. Biomol Ther (Seoul) 26:19–28
25. Effenberger M, Bommert KS, Kunz V, Kruk J, Leich E, Rudelius M, Bargou R, Bommert K (2017) Glutaminase inhibition in multiple myeloma induces apoptosis via MYC degradation. Oncotarget 8:85858–85867
26. Zhou R, Pantel AR, Li S, Lieberman BP, Ploessl K, Choi H, Blankemeyer E, Lee H, Kung HF, Mach RH, Mankoff DA (2017) [^{18}F](2S,4R)4-fluoroglutamine PET detects glutamine pool size changes in triple-negative breast cancer in response to glutaminase inhibition. Cancer Res 77:1476–1484
27. Dang CV (2012) MYC on the path to cancer. Cell 149:22–35
28. Liu YL, Lu MY, Chang HH, Lu CC, Lin DT, Jou ST, Yang YL, Lee YL, Huang SF, Jeng YM, Lee H, Miser JS, Lin KH, Liao YF, Hsu WM, Tzen KY (2016) Diagnostic FDG and FDOPA positron emission tomography scans distinguish the genomic type and treatment outcome of neuroblastoma. Oncotarget 7:18774–18786
29. Ni Y, Zhou Y, Zhou M, Zhang L (2015) Akt and cAMP response element binding protein mediate 17beta-estradiol regulation of glucose transporter 3 expression in human SH-SY5Y neuroblastoma cell line. Neurosci Lett 604:58–63
30. Ploessl K, Wang L, Lieberman BP, Qu W, Kung HF (2012) Comparative evaluation of ^{18}F-labeled glutamic acid and glutamine as tumor metabolic imaging agents. J Nucl Med 53:1616–1624
31. Maris JM (2010) Recent advances in neuroblastoma. N Engl J Med 362:2202–2211
32. Shimizu K, Kaira K, Tomizawa Y, Sunaga N, Kawashima O, Oriuchi N, Tominaga H, Nagamori S, Kanai Y, Yamada M, Oyama T, Takeyoshi I (2014) ASC amino-acid transporter 2 (ASCT2) as a novel prognostic marker in non-small cell lung cancer. Br J Cancer 110:2030–2039